High-Resolution Ultrasonic Imaging of Artworks with Seismic Interferometry for Their Conservation and Restoration

Draganov, Deyan; Hunziker, Jürg; Heller, Karel; Gutkowski, Karin; Marte, Fernando

DOI
10.1080/00393630.2018.1437870

Publication date
2018

Document Version
Accepted author manuscript

Published in
Studies in Conservation

Studies in Conservation

High-resolution Ultrasonic Imaging of Artworks/Artefacts with Seismic Interferometry for Their Conservation and Restoration

--Manuscript Draft--

Manuscript Number:	SIC590R3
Full Title:	High-resolution Ultrasonic Imaging of Artworks/Artefacts with Seismic Interferometry for Their Conservation and Restoration
Article Type:	Original Research or Treatment Paper
Keywords:	Seismic Interferometry; Transverse waves; Ultrasonic; Imaging; Artefacts; Artworks; Conservation; Restoration
Corresponding Author:	Deyan Draganov, Ph.D. Delft University of Technology Delft, NETHERLANDS
Corresponding Author Secondary Information:	
Corresponding Author's Institution:	Delft University of Technology
Corresponding Author's Secondary Institution:	
First Author:	Deyan Draganov, Ph.D.
First Author Secondary Information:	
Order of Authors:	Deyan Draganov, Ph.D.
	Jürg Hunziker, Dr.
	Karel Heller
	Karin Gutkowski, Dr.
	Fernando Marte, Dr.
Order of Authors Secondary Information:	
Abstract:	Artworks are an inseparable part of our cultural heritage of societies and provide us with a unique look at cultural developments through time and space. For the best possible conservation, it is paramount to know the constituent materials, condition, and construction techniques of the objects (e.g., painting on wood, fresco, sculpture). Such information is required not only at the surfaces of the objects, but also inside of them; in the imaging discipline this is known as depth imaging. Here, we introduce a new method for non-invasive depth imaging as an alternative to traditional non-invasive methods when the latter cannot be used to obtain required information. We use ultrasonic transverse-wave transmission measurements and turn them into virtual reflection measurements. We achieve this by applying seismic interferometry with active sources. Obtaining reflection measurements by seismic interferometry allows us to apply an advanced imaging technique - prestack depth migration, as used in seismic exploration - to produce a high-resolution depth image of an object. We apply our method to ultrasonic data recorded on a mockup of a painting on a wooden support. We validate our method by comparing our results with an image from X-ray computed tomography.
Funding Information:	Netherlands Organization for Scientific Research (864.11.009) — Dr. Deyan Draganov

High-resolution Ultrasonic Imaging of Artworks With Seismic Interferometry for Their Conservation and Restoration

Abstract

Artworks are an inseparable part of our cultural heritage of societies and provide us with a unique look at cultural developments through time and space. For the best possible conservation, it is paramount to know the constituent materials, condition, and construction techniques of the objects (e.g., painting on wood, fresco, sculpture). Such information is required not only at the surfaces of the objects, but also inside of them; in the imaging discipline this is known as depth imaging. Here, we introduce a new method for non-invasive depth imaging as an alternative to traditional non-invasive methods when the latter cannot be used to obtain required information. We use ultrasonic transverse-wave transmission measurements and turn them into virtual reflection measurements. We achieve this by applying seismic interferometry with active sources. Obtaining reflection measurements by seismic interferometry allows us to apply an advanced imaging technique – prestack depth migration, as used in seismic exploration – to produce a high-resolution depth image of an object. We apply our method to ultrasonic data recorded on a mockup of a painting on a wooden support. We validate our method by comparing our results with an image from X-ray computed tomography.

Introduction

The interdisciplinary activity of art conservation aims at generating knowledge about the objects (e.g., structure and history), understanding the deterioration processes of their building materials, and implementing methods for adequate conservation and restoration.

A principal criterion governing conservation is minimum intervention, which seriously restricts the applicable examination techniques. The main orientation in sciences like physics and chemistry is the development of non-invasive techniques (Miliani, et al., 2010) sensitive to different phenomena. Examination of paintings on wood (Figure 1a), wall paintings, and sculptures employs mainly techniques to analyse an object’s surface. To see deeper inside an object, techniques like ultraviolet induced luminescence photography (Taft & Mayer, 2000), infrared reflectography (Pezzati, et al., 2004; Daffara, et al., 2009), X-ray radiography (Mottin, et al., 2007) and X-ray computed tomography (Casali & Bettuzzi, 2009) (CT) have been used. Each technique reveals different aspects of the object and each has its own limitations. For example, X-ray radiography compresses an object’s three-dimensional structural information into a two-dimensional image (Figure 1b). CT provides depth information (Figure 1b inset), but requires expensive, stationary equipment, and special precautions to minimize radiation-exposure risk to personnel. Furthermore, the narrow aperture of CT scanners prohibits investigation of objects with large dimensions. Non-destructive ultrasonic testing can also be used, e.g., for cavity-presence evaluation (Gosálbez, et al., 2006), but does not provide detailed three-dimensional structural information. In non-destructive testing, array measurements, i.e., measurements with multiple receiver points, are common (e.g., Hill and Dixon, 2014; Ohara et al., 2017), but might suffer from generation of waves (surface waves) that are undesired for high-resolution depth imaging of a material, as these waves lower the obtainable resolution.

In seismology, high-resolution three-dimensional subsurface images can be obtained using the active-source reflection method (Yilmaz, 1999). The reflection method uses surface sources and receivers and is applied at scales from a few metres to hundreds of kilometres. The method is graphically introduced in Figure 2. A source (the star) initiated at the surface gives rise to seismic waves that propagate in the subsurface. The waves are represented by the arrows crossed by multiple arcs. Some of the waves (in black) reflect from in the subsurface at boundaries between structures (e.g., layers) with different seismic properties (like seismic velocity and density) and are then recorded by surface receivers (the triangles). The recording is of the reflected waves is called reflection response. The waves might reflect in the subsurface one or multiple times. The recording procedure at the receivers is repeated for multiple active-source positions, i.e., by moving the position of the star. The reflection responses from all sources can be processed using techniques from exploration seismology to produce images of subsurface structures. In the case of Figure 2, the image of the subsurface structures will be the image of the subsurface layer.

To obtain a high-resolution image of the subsurface structures, the sources and receivers should be sufficiently many and sufficiently densely placed with respect to each other. For small objects, like some art works, a practical problem might arise. The size of the used sources might be such that receivers can be placed only certain distance away from the sources, thus limiting the imaging resolution, especially of the shallow structures. In the test case we show below, the source and receivers have diameters of 5 mm. Thus, a receiver can be placed no closer than 5 mm from a source, thus limiting severely the resolution of structures that are shallower than 5 mm from the surface.

Yet another practical problem can be the presence of surface waves – energy propagating along an object’s surface (illustrated in grey in Figure 2). These waves provide no reflection information of the object and are thus considered noise. The surface waves will likely be the strongest arrivals at surface receivers masking parts of the useful reflected waves and hampering successful imaging. Normally, surface waves are suppressed by filtering (Yilmaz, 1999). Such filtering is not a trivial task and quite often does not lead to good results, as it also damages the reflected waves as well.

Because of the above-mentioned obstacles, we propose an alternative application of the reflection-imaging method. We use transmission measurements, i.e., when receivers and active sources are placed on two parallel surfaces of an object to be investigated, for example on the top and bottom of a painting on wood, see Figure 1c. We transform the transmission measurements into virtual reflection measurements with virtual sources at the positions of the receivers using the method of seismic interferometry (SI) with active sources (Draganov, et al., 2007; Wapenaar, et al., 2011).

Generally, SI is known as the process of retrieving the seismic response (direct waves, surface waves, reflections, refractions) between two receivers from the crosscorrelation of recordings at the two receivers from sources effectively surrounding these two receivers (e.g., Campillo & Paul, 2003; Wapenaar & Fokkema, 2006; Wapenaar & Snieder, 2007; Brenguier, et al., 2008). When the receivers are at the surface of the earth for example, only sources in the subsurface are required, for example along a hemisphere that finishes with the earth's surface. The latter principle is graphically explained in Figure 3. Let us have a homogenous subsurface with one reflecting object in it (grey). Sources in the subsurface are present along the complete thick dashed black line. The individual waves (arrows) from sources (white stars) are recorded by the receivers (triangles). Let us crosscorrelate the recorded wave arriving directly from a source to the left receiver (direct arrival – dashed arrow) with the wave recorded at the right receiver after reflecting at the surface and at the object inside the medium (reflected arrival – continuous arrows). The crosscorrelation process effectively eliminates the common-travel path (dashed-arrow part). The crosscorrelation process is repeated for all source (white-star) positions. Consecutive summation of the separate correlations from all the sources retrieves a reflection arrival at the right receiver from a virtual source (black star) at the position of the left receiver.

When retrieval of specific events is of interest, e.g., reflected waves, on the bases of stationary-phase arguments it can be shown that sources are required only inside the stationary-phase region (lower dashed ellipse in Figure 3) for the event of interest (Snieder, 2004). The stationary-phase region is the region inside which a function, in our case the correlation results from the individual sources in Figure 3, shows very little variation (i.e., is nearly stationary). Consequently, with sources close to and at the surface where receivers are placed (upper dashed ellipse in Figure 3), mainly surface waves are retrieved. With sources and receivers placed on opposing sides, i.e., using transmission measurements, mainly reflection arrivals are retrieved; surface waves would hardly be retrieved (Draganov et al., 2007). We use this latter principle for surface-wave suppression in our method.

Another advantage of using SI to turn transmission measurements into reflection measurements with virtual sources at the position of the receivers is having receivers very close to the retrieved virtual source – 1 mm in the test case we show below.

SI by crosscorrelation assumes medium without wave-energy loss during the wave propagation (Wapenaar & Fokkema, 2006; Wapenaar, et al., 2011) due to intrinsic processes like internal friction of the material. However, ultrasonic waves propagating through solid objects usually experience intrinsic energy loss. Because of this, we use SI by multidimensional deconvolution or MDD (Wapenaar, et al., 2008; Wapenaar, et al., 2011). This SI technique can be applied to media with energy loss due to intrinsic processes and still retrieve reliable results.

In practice, the seismic-reflection method is most commonly applied with longitudinal waves (P-waves), i.e., waves for which the particle vibration is in the direction of propagation of the wave (see Figure 4a).

To apply the method to artworks to image their internal structures, the used wavelength (i.e., the spatial period of the wave) should be shorter or comparable to the size of an object's internals. As the resolution increases with a decrease of the wavelength, sufficiently high frequencies should be used to achieve a high imaging resolution. For the test case below, we use ultrasonic frequencies although using high frequencies alone might not solve the problem. The P-wave velocities inside artworks could result in wavelengths not providing the required resolution. With relatively higher P-wave velocities, like in metal or wood, the wavelengths might also be relatively long. For the case of wood, for example, to see annual-growth rings as separate structures, the wavelength should be shorter than four times the distance between neighbouring rings.

To obtain higher spatial resolution, we make use of reflected transverse waves (S-waves), because for the same material, they are characterized by lower velocities than the P-waves. This means that for a source signal characterized by the same centre frequency, the S-wave would have a shorter wavelength than the P-waves as the former are characterized by a lower velocity. The S-waves are waves for which the particle vibration is in a direction perpendicular to the direction of the propagation of the wave, see Figures 4b and 4c. If a wave propagates in a horizontal direction, one can have S-waves whose particles vibrate (i.e., are polarized) in the vertical direction and thus commonly labelled SV-waves, see Figure 4b. An S-wave could also be polarized in the second horizontal direction. Such a wave is commonly labelled SH-wave, see Figure 4c. Both SV- and SH-waves are characterized by the same velocity if a material is characterized by the same properties in all spatial directions.

To record reflected SV-waves at the surface of an object, transducers sensitive to particle vibration in the vertical direction are used. Such transducers will also sense P-waves, converted at an objects internal structure boundary from SV-waves. This means that the same reflector inside an object will give rise to two recorded reflection arrivals. They are recorded at different times, because the velocity of the two wave types is different. Applying imaging to such recordings could lead to artificial (double) structures in the final images.

To avoid this, we use transducers sensitive to the particle vibration in the horizontal direction sensing SH-waves. An advantage of using SH-waves is that in a 2D geometry, when the source line is vertically below the receiver line and forms one plane with it, the SH-waves decouple from the P- and SV-waves. This suppresses the recording of converted waves. Nevertheless, P- and converted waves might still be recorded due to 3D scattering.

Mockup and Analysis

To demonstrate our method, we record ultrasonic data on a mockup imitating a painting on a wooden support (Figure 1c). The base of the mockup is made of 100-years-old, 21-millimetre-thick poplar wood. The base is covered with three layers: bottom – chalk and glue; middle – titanium white oil; top – calcined iron oxide. The mockup imposes high requirements on the resolution of the imaging methods to be used because of the mockup's thinness, the very short distance between the wood's annual-growth rings, and the small size of the possible damages inside the wooden support. For conservation, it is important to know: condition of the wooden support (degradation position and dimensions); if and where the chalk-and-glue layer detaches from the wood. The shorter sides of the mockup (insets in Figure 1c) reveal multiple wormholes and growth rings at the bare side (right inset) and only growth rings at the side covered with all three layers (left inset).

As sources and receivers, we use Fuji Ceramics piezoceramic transducers with a diameter of 5 mm. For having good contact with the material, and thus minimal loss of signal energy due to contact, we couple the transducers to the mockup using an S-wave couplant. We place the receivers along the Plexiglas-covered measuring tape (Figure 1c; the blue triangles in Figure 5a). In a real painting on wood, the receivers would be placed on the top iron-oxide layer, which is very smooth and would provide good coupling. The mockup's iron-oxide layer is rough and, thus, we place the receivers on the smooth oil layer (top of mockup). The impulsive source transducers (e.g., the blue star in Figure 5a) are placed on the opposite side (bottom) of the mockup vertically below (accuracy of 0.5 mm) the receivers. The transducers are sensitive to SH-waves, i.e., particle vibration as in Figure 4c. The thickness of the mockup between the sources and the receivers is 23 mm.

For real artworks, possible damage due to using the S-wave couplant to attach the transducers should be avoided. This could be achieved if the investigation area is covered with gel film based on methylcellulose (Doherty, at al., 2011). Another possibility might be the utilization of non-contacting laser ultrasonic equipment, using lasers as both sources and receivers (e.g., Nishizawa, et al., 1997; Draganov et al., 2007; Blum, et al, 2010). Note that when using laser source, the intensity must be sufficiently low to avoid damage to the objects. Yet another possibility might be the utilization of air-coupled transducers. In this case, though, only P-waves will be recorded, as S-waves do not propagate in air (fluids in general). This would mean recording of converted S-to-P-waves, but also P-waves propagating inside the mockup. The presence of such waves would make the interpretation of the final image difficult.

To record ultrasonic waves, we use a solid construct of a thin polyvinylchloride plate with eight receivers fixed in it every 6 mm (Figure 1c).

The receivers form one line. We perform the measurements as follows. We attach a source to the bottom of the mockup vertically below the receiver line's beginning, initiate the source, and record the transmission response along the array. To increase the ratio of the useful signal over the background non-repeatable electronic noise and vibration, the same measurement is repeated 128 times. The individual 128 recordings at each receiver are summed to obtain final recordings at eight receivers from this source position. The solid-construct array is then moved along the receiver line by 1 mm and a new recording from the same source is taken. The moving and recording is repeated five times. This produces transmission recordings at 48 receiver positions. We call the collection of these recordings a transmission common-source gather (CSG). After obtaining a complete transmission CSG, we move the source by 1 mm towards the receiver line's end and repeat the measurements. In total, we use 45 source positions resulting in 45 transmission CSGs.

Each source initiates an impulsive sine-wave signal with a centre frequency of 1 MHz. The signal is produced by an Agilent 33210A function generator, and is afterwards amplified by an ENI 2100 RF amplifier before being fed to the source (Figure 5a). The transmission responses are recorded on a Yokogawa DL9240 oscilloscope (Figure 5a) using a sampling rate of 20 ns.

Figures 5b,c show example transmission CSGs for sources at horizontal positions 76 mm and 99 mm, respectively. In both transmission panels, the earliest, and clearest, curved arrival is the direct transmitted SH-wave. The blue arrow in Figure 5a sketches a path of such an arrival. The direct transmitted SH-wave is followed by reverberations: some represent internal scattering at structural contrasts inside the mockup (the magenta arrow in Figure 5a); others represent reflections from the contrasts after the direct SH-wave has reflected at the top of the mockup (the cyan arrow in Figure 5a). The ringing horizontal arrivals earlier than the direct SH-wave are electromagnetic noise due to induction of the source signal to the receiver cables. Although this noise is weak, in the figure it appears relatively strong due to the signal amplification applied for visualization – at each receiver, the recorded transmission is amplified by normalizing the amplitude at each time sample with the root mean energy inside a running window of 0.01 ms centred at that time sample.

The transmission CSGs in Figure 5b,c are shown in travel time of the waves from the source to the receivers. This time can be transformed to travel-path distances if one knows the propagation velocities inside the object. Alternatively, one can estimate the average SH-wave velocity through the mockup using the thickness of 23 mm and the travel time of the direct SH-wave between a vertical source-receiver pair. As this velocity is useful, we estimate it by extracting the recording from each vertical source-receiver pair, summing these recordings to improve the signal-to-noise ratio, picking the time of the first arrival – the direct SH-wave, and dividing the mockup's thickness by the picked time. In this way, we estimate an average velocity of 1520 m/s. The wavelength for this velocity is 1.52 mm, theoretically allowing imaging/interpretation of structures separated by 0.5 mm. This theoretical value stems from the requirement to have two consecutive reflection arrivals in a recording separated by at least quarter of a wavelength (Yilmaz, 1999). We take here a third as a safer criterion.

The initiated signals' centre frequency of 1 MHz is not necessarily the centre frequency of the recorded signals. Figures 6a,b show the amplitude spectra of the CSGs from Figures 5b,c, respectively: the main energy of the recorded signals peaks between 800 kHz and 900 kHz and quickly weakens away from the receivers closest vertically above the source. The lower peak frequency and the loss of energy away from the source evidence intrinsic energy loss.

Reflection imaging of the mockup: a modelling example

We perform numerical-modelling tests to show what could be obtained using the reflection-imaging method in general. We simulate reflection measurements using a two-dimensional finite-difference modelling code (Thorbecke & Draganov, 2011). We create a numerical density model (Figure 7a) of the mockup between the source and receiver lines seen inside the yellow rectangle in Figure 5a. The colours indicate the density values inside layers (representing thickness between annual rings) and scatterers (e.g., wormholes): white – density of 10 kg/m^3; light grey – 650 kg/m^3; medium grey – 850 kg/m^3; dark grey – 1000 kg/m^3; black – 1050 kg/m^3. We keep the velocity constant at 1520 m/s, which is the estimated average velocity of the SH-waves.

To show a best-possible imaging scenario, we do not model surface waves. As explained above, these waves are considered noise. Furthermore, we do not model the top of the mockup as a free boundary. In the case for the laboratory measurements, due to the air above the mockup, the top of the mock up is a free boundary. Having a free boundary will totally reflect a wave incident at that boundary back inside the object resulting in recording reverberations (free-surface multiple reflections) between the seismic-property contrasts inside the mockup and the top of the mockup. Recorded free-surface multiples lead to artificial structures in the obtained image. Specially developed processing techniques aim at eliminating free-surface multiples from data. By not modelling a free boundary, we do not need to apply such techniques.

We further increase the resolution of the imaging, especially of deeper structures, by not modelling energy loss due to intrinsic processes.

We model receiver responses at the actual receiver positions. We simulate reflection measurements by placing a source at each receiver position. We use an impulsive source signal characterized by a Ricker wavelet (Ricker, 1952) with a centre frequency of 1 MHz. Figures 7c,d,e show simulated reflection CSGs for a source (the star) at 53 mm, 70 mm, and 90 mm, respectively. The vertical axis is expressed in the time waves propagate from a source to the receivers – reflected waves' two-way travel time. We indicate the reflection from the bottom of the first layer (R1), from the bottom of the mockup (R2), from scatterer 1 (Sc1) and from scatterer 3 (Sc3).

To obtain a depth image (Figure 7b) of the numerical model, we apply to the simulated reflection CSGs from all source positions prestack depth migration (Thorbecke et al., 2004). Migration is an algorithm that uses a velocity model to collapse the reflection arrivals to their corresponding reflection points inside objects (Yilmaz, 1999), in our case inside the mockup. We use a homogeneous velocity model of 1520 m/s. We see that the different layer boundaries are imaged at their exact places. Close to the receiver-line ends, the amplitudes of the imaged boundaries are lower because there less reflection CSGs contribute to the final image. The top and bottom of the five scatterers are delineated by vertical pair of events curved to a different degree (e.g., the black pointers in Figure 7b). The dominant wavelength of the modelled waves is 1.52 mm. This wavelength is comparable with the diameter of between 1 mm and 2 mm of the visible wormholes in the mockup, meaning the wormholes will be imaged as reflecting objects with limited dimensions. How much of the top and bottom of a scatterer is imaged depends on the illumination of that scatterer. The illumination, in turn, depends on the source/receiver positions and on the layering inside the mockup. For example, Sc1 and Sc4 are imaged at their top right parts clearly, which indicates that these two scatterers are being illuminated mainly from the right. The bottom left part of Sc4 is partly interpretable, but that is hardly possible for Sc1, showing that the receivers recorded very little reflected energy from the bottom of Sc1. For the other three scatterers, the illumination of the top left and right parts is more balanced; for Sc3 and Sc5, also the bottom parts are interpretable.

After showing the quality of the reflection image that could be obtained with the idealized numerical model and acquisition above, we introduce the method we want to use and show the results we obtain from the laboratory data of the mockup.

Method

In Appendix A, we explain the theory of the method we use. There, we introduce the symbols that we also use in this section.

Figures 5b,c show the transmission CSGs, what we also call transmission response $T^v(\mathbf{x}_B, \boldsymbol{x}^{\boldsymbol{i}}, t)$ in Appendix A, smeared by the source time function (STF), i.e., the length in time of the source signal, observed at the 48 receiver positions ($\mathbf{x}_B$ from (53,0) to (100,0) mm) from a source $\mathbf{x}^{\boldsymbol{i}}$ at positions (76,23) mm and (99,23) mm, respectively; t indicates time; and v in the superscript – that particle velocity was recorded. Using the transmission responses, we can retrieve the reflection response R^v with SI by crosscorrelation as explained in the Introduction; see Appendix A for a mathematical explanation. Even though we feed a sine wavelet to the sources, the STFs are elongated in time because we use unshielded transducers causing reverberations of the sine wave inside the transducers themselves. Having long STFs would result in lower-resolution images – the reflecting boundaries will appear thicker in the image. Ideally, knowing (measuring) a source's STF allows removing it using a process known as wavelet deconvolution. But measuring individual STFs at ultrasonic scales is difficult, and only estimates that approximate the true STFs could be obtained. Using the estimates instead of the true STFs might again lower the resolution. Because of this, we choose to retrieve the reflection response using other SI methods – by crosscoherence and MDD, as these two methods eliminate the STFs (see Appendix A).

We first apply SI by crosscoherence (relation A3 in Appendix A). As the transmission recordings suffer from energy loss due to intrinsic processes, the later reflections retrieved using crosscoherence would be unrealistically weak relative to the earlier reflections. Furthermore, next to the retrieved physical reflections, also non-physical reflections would be retrieved (Draganov, et al., 2010; Draganov, et al., 2012; King & Curtis, 2012). Non-physical reflections are retrieved events that cannot be recorded using a physical source at the position of the virtual source. Non-physical events are undesired, as they deteriorate the imaging quality. Attempting to increase the amplitude of possible retrieved later reflections, we amplify the recorded transmission CSG, effectively trying to compensate for the intrinsic energy loss. The best amplification depends on an object's energy attenuation. Not having an estimate of the attenuation, we test amplifying the data by multiplying the signal's amplitude at each time sample by t, t^2, t^3. For our dataset, the best results appear to be the ones using t^3.

Figure 8(a) shows the retrieved R^v, or as explained in Appendix A – the crosscoherence function **Cch,** using the amplified transmission CSGs $T^v(\mathbf{x}_B, \boldsymbol{x^i}, t)$ (Figures 5b,c). The virtual source is at $\mathbf{x}_B = (75,0)$ mm, the receivers – at multiple positions $\mathbf{x}_A = (53,0)$ to $\mathbf{x}_A = (100,0)$ mm. As relation (A3) predicts, both positive and negative times are retrieved in Figure 8a. If the source array were sufficiently long, the retrieved reflection response at positive and negative times would have been the same, and we could have taken the positive times to obtain the complete retrieved reflection response. For a horizontally layered mockup, sufficiently long would mean extending the source array on each side of the receiver array by more than half the length of the receiver array.

For our source-receiver geometry and the complex internal structure of the mockup, due to stationary-phase considerations (Snieder, 2004), some parts of R^v would be better retrieved at positive times, other parts – at negative times. As the mockup is strongly heterogeneous, using only the source-receiver geometry it is not easy to decide, like for a horizontally layered mockup, which times should be selected. Because of this, we compare visually the quality of the retrieved positive and negative times. From the comparison, we decide for virtual-source positions from $\mathbf{x}_B = (67,0)$ to $\mathbf{x}_B = (86,0)$ mm to select the positive times and discard the negative times (Figure 8b). For virtual-source positions from $\mathbf{x}_B = (53,0)$ to $\mathbf{x}_B = (67,0)$ mm, we take the time-reversed negative times for receivers to the right of the virtual source and concatenate them to the positive times taken for receivers to the left of the virtual-source position (Figure 8c). For virtual-source positions from $\mathbf{x}_B = (86,0)$ to $\mathbf{x}_B = (100,0)$ mm, we do the opposite (Figure 8d).

In an active-source experiment with pure SH-waves, nothing would propagate faster inside the mockup than the direct SH-wave and possibly a refracted wave at longer offsets. This means that in the retrieved virtual CSGs events earlier than the expected direct SH-wave would be artificial, except for possible retrieved refractions. Because of this, we set to zero everything earlier than the expected direct SH-wave. Note that for reflection imaging, the refracted arrivals are undesired and can also be set to zero.

Figure 9a shows the final retrieved reflection CSG for a virtual source at $\mathbf{x}_B = (75,0)$ mm. The pointers indicate possible retrieved reflections from the seismic-property contrasts inside the mockup. Comparison with the numerically modelled response shows that these events might indeed be retrieved reflections. We also see that the retrieved events are interpretable only at earlier times, but even at these times not interpretable along the complete receiver line. The partial retrieval of reflection events along the line might be due to less-then-optimal illumination from the active sources. Note that because of the energy attenuation, some of these events might actually be retrieved non-physical reflections.

We now apply SI by MDD using equation (A7) and equation (A8) for $\Gamma_{cch}^{\tau_{yz}}$. The latter is a multidimensional factor estimated from the measured data that tries to correct the less-then-optimal result $\mathbf{Cch}$ for its shortcomings. To perform the inversion in equation (A7), we need to estimate $\Gamma_{cch}^{\tau_{yz}}$ and $\mathbf{Cch}$. We estimate them from SI by crosscoherence (equation (A3)), but without applying time-dependent amplification to the transmission CSGs. Figure 10a shows the result for a virtual source at (75,0) mm. The result is dominated by events passing through the virtual-source position at time 0 s. These events are obtained from the crosscoherence of arrivals that would be recorded by the receivers in the absence of a free boundary at the top of the mockup. Keeping only the retrieved arrivals passing through the virtual-source position at time 0 s and the arrivals around them as in the example in Figure 10b (see Wapenaar et al. (2011) for details on why keeping only these arrivals), we obtain an approximation Γ_{cch}^{v} for measurements of the particle velocity v instead of $\Gamma_{cch}^{\tau_{yz}}$ for measurements of the shearing stress τ_{yz}. Isolating the result in Figure 10b from the complete result Figure 10a gives an approximation of $\mathbf{Cch}$ (Figure 10c) as required for the inversion of equation (A7).

To estimate $\Gamma_{cch}^{\tau_{yz}}$ from Γ_{cch}^{v}, we use the following. In the absence of a free surface at the level of the receivers, the wavefields recorded at the receivers continue travelling away from them. In such a case, a shearing-stress recording (τ_{yz}) at the receivers can be shown to be proportional to v_y. This relation can be obtained using the elastic equivalent of the acoustic equation of motion. When the seismic parameters just below the receivers do not change (like in our case of a chalk-and-glue layer), the proportionality factor is one over the cosine of the angle between the propagation direction of the first arrival at the virtual-source position with respect to the receiver surface. We approximate this angle by the angle between the vertical and the line connecting the virtual- and active-source positions. We further assume that particle-velocity recording in the absence of a free surface at the receivers can be obtained from the particle-velocity recording in the presence of a free surface by windowing.

Results and Discussion

We retrieve reflection CSGs using SI by crosscoherence and by MDD for virtual sources at all receiver positions. We then apply band-pass filter between 0.4 MHz and 1.2 MHz (Figures 9a,b). The crosscoherence result exhibits interpretable possible retrieved reflections until about 0.01 ms (the pointers in Figure 9a), while in the MDD result the later possible retrieved reflections are more interpretable (the pointers in Figure 9b). The reason for this might be that SI by MDD takes wave-energy loss due to intrinsic processes into account and/or that it (partly) compensates for possible illumination inhomogeneity. On the other hand, the less-than-optimal estimation of $\Gamma_{cch}^{\tau_{yz}}$ might be the reason for not seeing earlier events in the SI-by-MDD result.

After retrieving all reflection responses, we apply prestack depth migration (Thorbecke et al., 2004) to obtain a depth image of the mockup under the receiver line. For the migration, we use a homogeneous velocity of 1520 m/s as estimated from the transmission measurements as described above. Figures

11a,b show the depth images of the mockup obtained from the MDD and crosscoherence results, respectively. After migration, we apply an extra high-cut filter at 1 MHz to improve interpretability. For comparison, in Figure 11c we show the part of the X-ray CT image of the mockup inside the yellow rectangle in Figure 5a.

The SI images in Figure 11 exhibit inclined linear events, starting at the left and right sides and dipping to the centre, not present in the CT image. These are artificial events because of the limited aperture, due to both SI and imaging, which could be suppressed by using longer acquisition geometry. The CT image (Figure 11c) shows that the chalk-and-glue layer is thick between 2 mm and 1 mm at horizontal distance 53 mm and 100 mm, respectively. In both SI images, the bottom of the chalk-and-glue layer is partly imaged at such depths.

Inside the wooden support, the SI-by-MDD image (Figure 11a) reveals in general a superior picture than the SI-by-crosscoherence image (Figure 11b). The SI-by-MDD image is less noisy and more continuous in the lateral direction. This allows for an easier interpretation of the wooden support’s structure, with the most prominent feature being the dome-like feature of several layers with an apex around (85,5) mm. This feature and a few other clearly interpretable seismic-property contrasts in the SI-by-MDD image are the annual-growth rings imaged in the CT image as well.

The CT image reveals five scatterers, marked by the orange crosses in Figure 11c. Scatterers Sc1 to Sc4 are wormholes. The nature of Sc5 is unclear, but it might be a density contrast. As explained in the modelling example, the presence of the scatterers would be evidenced by vertical pairs of curved events.

In the SI-by-MDD image, Sc3 and Sc5 are indicated by the presence of the lower part of the curved pair of events, and could be interpreted as scatterers. In the SI-by-crosscoherence image, the vertical pair is present for Sc5. The absence of the upper event for Sc5 in the SI-by-MDD image might be coming from the less-than-optimal estimation of $\Gamma_{cch}^{\tau_{yz}}$. Even though parts of some of the scatterers in the SI images could be interpreted, the signal-to-noise ratio of the pair of curved events is low, which makes the interpretation of the scatterers difficult. The signal-to-noise ratio, and thus interpretability, could be increased if 2D acquisition geometry of source and receiver transducers is used. For example, this might mean using several lines of source and of receiver transducers instead of the single line of source and single line of receiver transducers we use. Using 2D acquisition would also allow obtaining a 3D image of the mockup from 3D migration. This will further remove possible ambiguity in a 2D image that might arise from migration of reflection or scattering events not inside the plane of the source and receiver lines we use. When using 2D acquisition, to avoid the appearance of strong converted and P-waves, care should be taken to record the transmission response from a source transducer only at receiver lines that are close to lying vertically above that source transducer.

To compare the resolution of the SI images to that from the CT scan, we overlay the latter with each of the SI images (Figures 12a,b). The overlays show that SI by MDD has imaged the annual-growth rings at the same depth as the CT image. The resolution of the two images is also comparable. Where the CT image shows strong annual-growth ring contrasts, the SI-by-MDD image shows them as well. In Figure 12c, we overlay the CT scan with an image obtained from the summation of the SI-by-crosscoherence and SI-by-MDD images. We can see that taken complementary, the two SI images provide a nearly complete image of the chalk-and-glue layer.

We compare our results to a CT image, but obtaining a CT image requires expensive, stationary equipment and special precautions. The application of CT is also limited by the aperture of the CT scanner. Our method can be used with off-the-shelf mobile equipment and can be applied even to large artworks for imaging of areas of interest. On the other hand, a CT image can be obtained of objects with any roughness of the surfaces. Rough surfaces might cause poor transducer/object contact thus limiting the utilization of ultrasonic measurements.

The validation of our results with the CT image shows that our method can provide high-resolution information of the material structure and condition of artworks and thus be a valuable new tool for non-invasive depth characterization for conservation and restoration purposes.

Conclusions

We proposed a new non-invasive ultrasonic method for high-resolution depth imaging of artworks. The method uses transmission measurements of transverse waves. The shorter wavelength of the transverse waves, compared to longitudinal waves for the same frequencies, contributes to the higher spatial resolution. Our method makes use of seismic interferometry by multidimensional deconvolution to turn the transmission measurements into reflection measurements from virtual sources at the receiver position. Retrieving reflections from transmissions suppresses retrieval of surface waves, which normally are present in actual reflection data and interfere with it. Application of seismic interferometry by multidimensional deconvolution also results in the compaction of the source wavelet and thus increases the resolution of the final ultrasonic image. Having obtained reflection measurements allows application of advanced seismic imaging techniques as used in the seismic-exploration industry. We applied our method to a mockup antique painting consisting of a 21-millimetre-thick wooden support of about 100-years-old poplar wood, a bottom layer of chalk and glue, a middle layer of titanium white oil, and a top layer of calcined iron oxide. We performed transmission measurements with receivers on the titanium-white-oil layer and sources vertically below them on the opposite side of the mockup. From the measured transmission data, we retrieved virtual reflections, to which we consecutively applied prestack depth migration to obtain a depth image of the mockup. The ultrasonic image revealed the base of the chalk-and-glue layer, and inside the wooden support – annual-growth rings and scatterers, like wormholes. Comparing our results to an image from X-ray computed tomography, we confirmed that our method has imaged the structures inside the mockup at the same depth and with resolution comparable to that of the computed-tomography image. The validation shows that our method can provide high-resolution information of the material structure and condition of artworks and can be a valuable new tool for non-invasive characterization in depth.

Appendix A

We introduce the basics of reflection retrieval from transmissions using SI by crosscorrelation, crosscoherence, and MDD.

Let $R^v(\mathbf{x}_A, \mathbf{x}_B, t)$ denote the impulse reflection response at a receiver at $\mathbf{x}_A$ from an impulsive source at $\mathbf{x}_B$, the superscript v indicating that particle velocity is recorded, and $\mathbf{x} = (x, y, z)$, where axis x is oriented along the receiver line on the mockup, y – across the line, and z – in the vertical direction. $T^v(\mathbf{x}_A, \boldsymbol{x}^{\boldsymbol{i}}, t)$ and $T^v(\mathbf{x}_B, \boldsymbol{x}^{\boldsymbol{i}}, t)$ denote transmission responses measured at receivers at $\mathbf{x}_A$ and $\mathbf{x}_B$, respectively, from an impulsive source at $\mathbf{x}^{\boldsymbol{i}}$. The reflection and the transmission responses are related (Wapenaar & Fokkema, 2006) through

$$\{R^v(\mathbf{x}_A, \mathbf{x}_B, t) + R^v(\mathbf{x}_A, \mathbf{x}_B, -t)\} * S_{av}(t)$$
$$\propto \sum_i \{T^v(\mathbf{x}_B, \mathbf{x}^{\boldsymbol{i}}, -t) * T^v(\mathbf{x}_A, \mathbf{x}^{\boldsymbol{i}}, t) * s(\mathbf{x}^{\boldsymbol{i}}, -t) * s(\mathbf{x}^{\boldsymbol{i}}, t)\}, (A1)$$

where $s(\mathbf{x}^{\boldsymbol{i}}, t)$ is the source time function (STF) of the source at $\mathbf{x}^{\boldsymbol{i}}$ and $S_{av}(t)$ is the average of the autocorrelated STFs. The asterisk denotes convolution, but convolution between time-advanced and time-retarded signals is equal to correlation. The above relation is SI by crosscorrelation and shows how to retrieve the reflection response at $\mathbf{x}_A$ due to a virtual source at $\mathbf{x}_B$. Equation (A1) assumes a medium without energy attenuation caused by intrinsic processes, source boundary in the far field of the receivers, smoothly varying medium parameters across the boundary, and includes a high-frequency approximation.

In the frequency domain, the convolutions of equation (A1) become multiplications:

$$\{R^v(\mathbf{x}_A,\mathbf{x}_B,\omega)+\left(R^v(\mathbf{x}_A,\mathbf{x}_B,\omega)\right)^*\}S_{av}(\omega)$$
$$\propto \sum_i \left\{\left(T^v(\mathbf{x}_B,\mathbf{x}^i,\omega)\right)^* T^v(\mathbf{x}_A,\mathbf{x}^i,\omega)\left(s(\mathbf{x}^i,\omega)\right)^* s(\mathbf{x}^i,\omega)\right\}, (A2)$$

where the asterisk in a superscript indicates complex conjugation, and ω denotes angular frequency. If the right-hand side (RHS) is divided by the amplitude spectrum of the transmission measurements at $\mathbf{x}_A$ and $\mathbf{x}_B$, the denominator will contain the square of the STF's amplitude spectrum. The multiplication of the STF with its complex conjugate in the RHS is also equal to the square of the STF's amplitude spectrum. Thus, applying SI by crosscorrelation to the transmission measurements normalized by their amplitude spectrum, we obtain SI by crosscoherence (Nakata, et al., 2011):

$$R^v(\mathbf{x}_A,\mathbf{x}_B,\omega)+\left(R^v(\mathbf{x}_A,\mathbf{x}_B,\omega)\right)^*$$
$$\propto \sum_i \left\{\frac{\left(T^v(\mathbf{x}_B,\mathbf{x}^i,\omega)\right)^* T^v(\mathbf{x}_A,\mathbf{x}^i,\omega)}{|T^v(\mathbf{x}_B,\mathbf{x}^i,\omega)||T^v(\mathbf{x}_A,\mathbf{x}^i,\omega)|}\right\}, \qquad (A3)$$

where | | denotes amplitude spectrum. As can be seen, the advantage is that the STFs are completely removed. The disadvantage is that for $\mathbf{x}_A=\mathbf{x}_B$, in the numerator in the RHS of equation (A3) one obtains the square of the amplitude spectrum of the measured transmission response, which is subsequently removed by division with itself; this division eliminating completely the reflection information (clamped boundary condition; Vasconcelos & Snieder, 2007).

As SI by crosscoherence is derived from SI by crosscorrelation, it inherits the same assumptions.

SI by crosscorrelation and crosscoherence aim to retrieve the impulse reflection response. This can be achieved when there is no energy attenuation in the medium and when the sources illuminated the receivers homogeneously from all directions. In field or laboratory measurements, such situations would be very difficult to achieve. Because of this, it is better to say that instead of $R^v(\mathbf{x}_A, \mathbf{x}_B, \omega)$ the correlation $\mathbf{Ccr}(\mathbf{x}_A, \mathbf{x}_B, \omega)$ or coherence function $\mathbf{Cch}(\mathbf{x}_A, \mathbf{x}_B, \omega)$ is retrieved. Wapenaar et al. (2011) showed that $\mathbf{Ccr}(\mathbf{x}_A, \mathbf{x}_B^k, \omega)$ is connected to the actual impulse reflection response $R^v(\mathbf{x}_A, \mathbf{x}_C^j, \omega)$ through

$$\mathbf{Ccr}(\mathbf{x}_A, \mathbf{x}_B^k, \omega) = \sum_j R^v(\mathbf{x}_A, \mathbf{x}_C^j, \omega)\Gamma^p(\mathbf{x}_B^k, \mathbf{x}_C^j, \omega), \qquad (A4)$$

where k indicates multiple virtual-source positions, subscript C indicates a virtual-source position for the response Γ^p, p indicates measurements of acoustic pressure, and j is the number of receivers (virtual sources). As we use elastic medium with SH-waves, instead of the acoustic pressure we actually measure the shearing stress τ_{yz} of the traction vector $\boldsymbol{\tau}_z$ acting across a plane normal to the vertical axis z. So, we exchange p for τ_{yz}. The matrix

$$\mathbf{Ccr}(\mathbf{x}_A, \mathbf{x}_B^k, \omega) = \sum_i \left\{ \left(\bar{T}^v(\mathbf{x}_B^k, \mathbf{x}^i, \omega)\right)^* T^v(\mathbf{x}_A, \mathbf{x}^i, \omega) \left(s(\mathbf{x}^i, \omega)\right)^* s(\mathbf{x}^i, \omega) \right\}, (A5)$$

is identical, except for the bar above T, to the RHS of equation (A2). The bar indicates a measurement in a medium characterized by a homogeneous half space above the receivers (instead of having free surface). The matrix

$$\Gamma^{\tau_{yz}}(\mathbf{x}_B^k, \mathbf{x}_C^j, \omega) = \sum_i \left\{ \left(\bar{T}^{\tau_{yz}}(\mathbf{x}_B^k, \mathbf{x}^i, \omega)\right)^* \bar{T}^{\tau_{yz}}(\mathbf{x}_C^j, \mathbf{x}^i, \omega) \left(s(\mathbf{x}^i, \omega)\right)^* s(\mathbf{x}^i, \omega) \right\}, (A6)$$

practically shows how far the correlation function $\mathbf{Ccr}$ is from R^v. As both $\mathbf{Ccr}$

and $\Gamma^{\tau_{yz}}$ can be estimated from measured data, equation (A4) can be solved for R^v by matrix inversion. This process is known as SI by MDD. In our case, we use stabilized least-squares inversion (e.g., Wapenaar, et al., 2011).

Equation (A4) is written for crosscorrelation, but can similarly be written for crosscoherence:

$$\mathbf{Cch}\left(\mathbf{x}_A, \mathbf{x}_B^k, \omega\right) = \sum_j R^v\left(\mathbf{x}_A, \mathbf{x}_C^j, \omega\right)\Gamma_{cch}^{\tau_{yz}}\left(\mathbf{x}_B^k, \mathbf{x}_C^j, \omega\right), \qquad (A7)$$

with

$$\Gamma_{cch}^{\tau_{yz}}\left(\mathbf{x}_B^k, \mathbf{x}_C^j, \omega\right) = \sum_i \left\{\frac{\left(\bar{T}^{\tau_{yz}}\left(\mathbf{x}_B^k, \mathbf{x}^{\boldsymbol{i}}, \omega\right)\right)^* \bar{T}^{\tau_{yz}}\left(\mathbf{x}_C^j, \mathbf{x}^{\boldsymbol{i}}, \omega\right)}{\left|\bar{T}^{\tau_{yz}}\left(\mathbf{x}_B^k, \mathbf{x}^{\boldsymbol{i}}, \omega\right)\right|\left|\bar{T}^{\tau_{yz}}\left(\mathbf{x}_C^j, \mathbf{x}^{\boldsymbol{i}}, \omega\right)\right|}\right\}. (A8)$$

References

Blum, T.E., van Wijk, K., Pouet, B. & Wartelle, A. 2010. Multicomponent wavefield characterization with a novel scanning laser interferometer. *Review of Scientific Instruments*, 81: 073101. doi:10.1063/1.3455213.

Brenguier, F., Shapiro, N. M., Campillo, M., Ferrazzini, V., Duputel, Z., Coutant, O. & Nercessian, A. 2008. Towards forecasting volcanic eruptions using seismic noise. *Nature Geoscience*, 1: 126-130.

Campillo, M. & Paul, A. 2003. Long-range correlations in the diffuse seismic coda. *Science*, 299: 547-549.

Casali, F. & Bettuzzi, M. 2009. In: D. Pinna, M. Galeotti and R. Mazzeo (Eds.), *Scientific Examination for the Investigation of Paintings. A Handbook for*

Conservator-Restores. Firenze: Centro Di.

Daffara, C., Fontana, R. & Pezzati, L. 2009, Scientific Examination for the Investigation of Paintings. In: D. Pinna, M. Galeotti, and R. Mazzeo, eds. *A Handbook for Conservator-restores*. Firenze: Centro Di.

Doherty, B., Brunetti, D. G., Sgamellotti, A. & Miliani, C. 2011. A detachable sers active cellulose film: a minimally invasive approach to the study of painting lakes. *Journal of Raman Spectroscopy*, 42: 1932-1938.

Draganov, D., Wapenaar, K., Thorbecke, J. & Nishizawa, O. 2007. Retrieving reflection responses by crosscorrelating transmission responses from deterministic transient sources: Application to ultrasonic data. *Journal of the Acoustical Society of America*, 122: EL172-EL178. doi:10.1121/1.2794864.

Draganov, D., Ghose, R., Ruigrok, E., Thorbecke, J. & Wapenaar, K. 2010. Seismic interferometry, intrinsic losses and Q-estimation. *Geophysical Prospecting*, 58: 361-373. doi:10.1111/j.1365-2478.2009.00828.x.

Draganov, D., Heller, K. & Ghose, R. 2012. Monitoring CO2 storage using ghost reflections retrieved from seismic interferometry. *International Journal of Greenhouse Gas Control*, 11S: S35-S46. doi:10.1016/j.ijggc.2012.07.026.

Gosálbez, J., Salazar, A., Bosch, I., Miralles, R. & Vergara, L. 2006. Application of ultrasonic nondestructive testing to the diagnosis of consolidation of a restored dome. *Materials Evaluation*, 64: 492-497.

Hill, S. & Dixon, S. 2014. Localisation of defects with time and frequency measurements using pulsed arrays. *NDT & E International*, 67: 24-30.

King, S. & Curtis, A. 2012. Suppressing nonphysical reflections in Green's function estimates using source-receiver interferometry. *Geophysics*, 77:

Q15-Q25.

Miliani, C., Rosi, F., Brunetti, B. G. & Sgamellotti, A. 2010. In situ noninvasive study of artworks: the MOLAB multitechnique approach. *Accounts of Chemical Research*, 43: 728-738.

Mottin, B., Martin, E. & Laval, E. 2007. Raphael's paintings in French museums: Some new results from recent technical investigations. In: A. Roy and M. Spring, eds. *Raphael's Painting Technique: Working Practices Before Rome.* Firenze: Nardini.

Nakata, N., Snieder, R., Tsuji, T., Larner, K. & Matsuoka, T. 2011. Shear wave imaging from traffic noise using seismic interferometry by cross-coherence. *Geophysics*, 76: SA97-SA106.

Nishizawa, O., Satoh, T., Lei, X. & Kuwahara, Y. 1997. Laboratory studies of seismic wave propagation in inhomogeneous media using laser dopler vibrometer. *Bulletin of the Seismological Society of America*, 87: 809–823.

Ohara, Y., Takahashi, K., Ino, Y., Yamanaka, K, Tsuji, t. & Mihara, T. 2017. High-selectivity imaging of closed cracks in a coarse-grained stainless steel by nonlinear ultrasonic phased array. *NDT & E International*, 91: 139-147.

Pezzati, L., Materazzi, M. & Poggi, P. 2004, Ir-colour scanning reflectography. In: B. Brunetti, C. Seccaroni and A. Sgamellotti, eds. *The painting technique of Pietro Vanunucci, called Il Perugino*. Firenze: Nardini.

Ricker, N. 1952. The form and laws of propagation of seismic wavelets. *Geophysics*, 18: 10-40.

Snieder, R. 2004. Extracting the Green's function from the correlation of coda waves: a derivation based on stationary phase. *Physical Review E*, 69:

046610.

Taft, J. & Mayer, J. W. 2000. *The Science of paintings*. New York: Springer-Verlag.

Thorbecke, J., Wapenaar, K. & Swinnen, G. 2004. Design of one-way wavefield extrapolation operators, using smooth functions in WLSQ optimization. *Geophysics*, 69: 1037-1045. doi:10.1190/1.1778246.

Thorbecke, J. & Draganov, D. 2011. Finite-difference modeling experiments for seismic interferometry. *Geophysics*, 76: H1-H18. doi:10.1190/GEO2010-0039.1

Vasconcelos, I. & Snieder, R. 2008. Interferometry by deconvolution, Part 1 – Theory for acoustic waves and numerical examples. *Geophysics*, 73: S115-S128.

Wapenaar, K. & Fokkema, J. 2006. Green's functions representations for seismic interferometry. *Geophysics*, 71: SI33-SI46. doi:0.1190/1.2213955.

Wapenaar, K. & Snider, R. 2007. Chaos tamed. *Nature*, 447: 643. doi:10.1038/447643a.

Wapenaar, K., Slob, E. & Snieder, R. 2008. Seismic and electromagnetic controlled-source interferometry in dissipative media. *Geophysical Prospecting*, 56: 419-434. doi:0.1111/j.1365-2478.2007.00686.x.

Wapenaar, K., van der Neut, J., Ruigrok, E., Draganov, D., H • unziker, J., Slob, E., Thorbecke, J. & Snieder, R. 2011. Seismic interferometry by crosscorrelation and by multidimensional deconvolution: a systematic comparison. *Geophysical Journal International*, 185: 1335-1364. doi:10.1111/j.1365-246X.2011.05007.x.

Yilmaz, O. 1999. *Seismic data processing*, 9th ed. Tulsa: SEG.

Figure Captions

Figure 1: **(a)** Painting on wood: Assumption of the Virgin (16th Century), private collection, Argentina. Photo: Tarea-IIPC. **(b)** X-ray photo of used mockup, which imitates painting on wood and consists of a wooden support, chalk-and-glue layer (beige), titanium-white-oil layer (white), and calcined-iron-oxide layer (brown). Inset shows a vertical slice of the mockup's X-ray computed tomography image along the receiver line. Yellow rectangle indicates the part of the mockup we image with our method. **(c)** The mockup. The two shorter sides shown in the insets. Orange circles indicating wormholes, orange arrows – annual-growth rings.

Figure 2: Principle of seismic reflection measurements. A source (white star) at the surface is initiated and gives rise to waves (lines with arcs) propagating in the subsurface. Some of the waves reflect at subsurface boundaries, like the grey layer, and are recorded at the surface by receivers (triangles). Such waves are called reflected waves (black lines and arcs). Other waves propagate only along the surface and are called surface waves (grey lines and arcs)

Figure 3: Principle of seismic interferometry (SI). Sources (white stars) are placed inside a homogenous medium along a boundary (thick dashed black line), which finishes at the surface. Two receivers (triangles) are placed at the surface. The medium contains only one reflecting object

(grey). Propagating waves are represented by the dashed and continuous arrows. The dashed ellipses indicate stationary-phase regions. After application of SI, the left receiver is turned into a virtual source (black star).

Figure 4: Explanation of wave types: **(a)** longitudinal (P-) wave – the particles (grey circles) vibrate in the direction of the propagation of the wave; **(b)** and **(c)** transversal (S-) waves – the particles vibrate in a direction perpendicular to the direction of the propagation of the wave. When the wave propagates along the x-coordinate axis, an S-wave with particle vibration **(b)** along the z-coordinate axis is called SV-wave, while **(c)** along the y-coordinate axis – SH-wave.

Figure 5: **(a)** Illustrative representation of setup. A sine signal from function generator is amplified and fed to a source transducer (star). Transmissions detected by receiver transducers (triangles) go to an oscilloscope. The transducers are sketched on the slice from the inset in Figure 1b. Coloured arrows illustrate travel paths of three arrivals (see main text). **(b)** and **(c)** Transmission common-source gathers for a source at the mockup's bottom at (76,23) mm and at (99,23) mm, respectively. For visualization, panels are clipped and the images in (b) and (c) are linearly interpolated to include an extra point between receivers. Before clipping, the recording at each receiver is normalized (see text).

Figure 6: Amplitude frequency spectrum of the transmission common-source gather shown **(a)** in Figure 3b and **(b)** in Figure 3c.

Figure 7: **(a)** Numerical model of the density inside the yellow rectangle in Figure 3(a). Five scatterers are marked by crosses/numbers. White colour stands for density of 10 kg/m^3, light grey – 650 kg/m^3, medium grey – 850 kg/m^3, dark grey – 1000 kg/m^3, and black – 1050 kg/m^3. **(b)** Image of the mockup's model obtained from migrating the simulated reflection measurements. Pointers indicate vertical pairs of events characteristic of scatterer. **(c)**, **(d), (e)** Simulated reflection common-source gathers for sources (stars) at (53,0) mm, (70,0) mm, and (90,0) mm, respectively. The reflection from the first layer's bottom is labelled R1, from the model's bottom – R2, from scatterers 1 and 3 – Sc1 and Sc3, respectively.

Figure 8: **(a)** Result from SI by crosscoherence for a virtual source at $\mathbf{x}_B = (75{,}0)$ mm obtained from amplified transmissions. **(b), (c), (d)** Illustration of which parts of the retrieved positive and negative times are used for a virtual source at $\mathbf{x}_B = (75{,}0)$ mm, $\mathbf{x}_B = (60{,}0)$ mm, and $\mathbf{x}_B = (90{,}0)$ mm, respectively. See main text for details. For visualization, the images are interpolated as in Figure 3b,c.

Figure 9: Reflection response **(a)** retrieved using SI by crosscoherence, **(b)** retrieved using SI by multidimensional deconvolution, and **(c)** simulated using the numerical modelling for a (virtual-)source co-located with the middle receiver. For visualization, the panels are clipped; the images in (a) and (b) are interpolated as in Figures 3b,c. The pointers indicate possible retrieved reflections.

Figure 10: **(a)** Result retrieved using SI by crosscoherence without amplifying the

transmissions for virtual source at $\mathbf{x}_B = (75{,}0)$ mm. **(b)** Selecting the dominant arrivals from (a) that pass through the virtual-source position at time 0 s. **(c)**. Result from the isolation of the events in (b) from the panel in (a). For visualization, the images are interpolated as in Figures 3b,c.

Figure 11: Depth image after migrating the reflections retrieved using SI by **(a)** multidimensional deconvolution and **(b)** crosscoherence. **(c)**. Image from X-ray computed tomography. Scatterers (e.g., wormholes) in the computed-tomography image indicated by orange crosses and numbered from 1 to 5. Example annual-growth rings indicated by pointers.

Figure 12: Overlay of the images from **(a)** Figure 9a and 9c and **(b)** Figure 9b and 9c. In **(c)** the result of the summation of the images from Figure 9a and 9b is overlaid on the image from Figure 9c. For a better contrast, the grey scale from Figure 9 is exchanged for black and white.

Acknowledgements

This research is supported by the Division for Earth and Life Sciences (ALW) with financial aid from the Netherlands Organization for Scientific Research (NWO) with grant VIDI 864.11.009. We thank two anonymous reviewers for their comments that helped improve the manuscript.

Figure 1

Click here to download Colour figure sc_2016_paintings_fig1.eps

Figure 2

Click here to download Non-colour figure sc_2016_reflection_seismics_explanation_fig2.eps

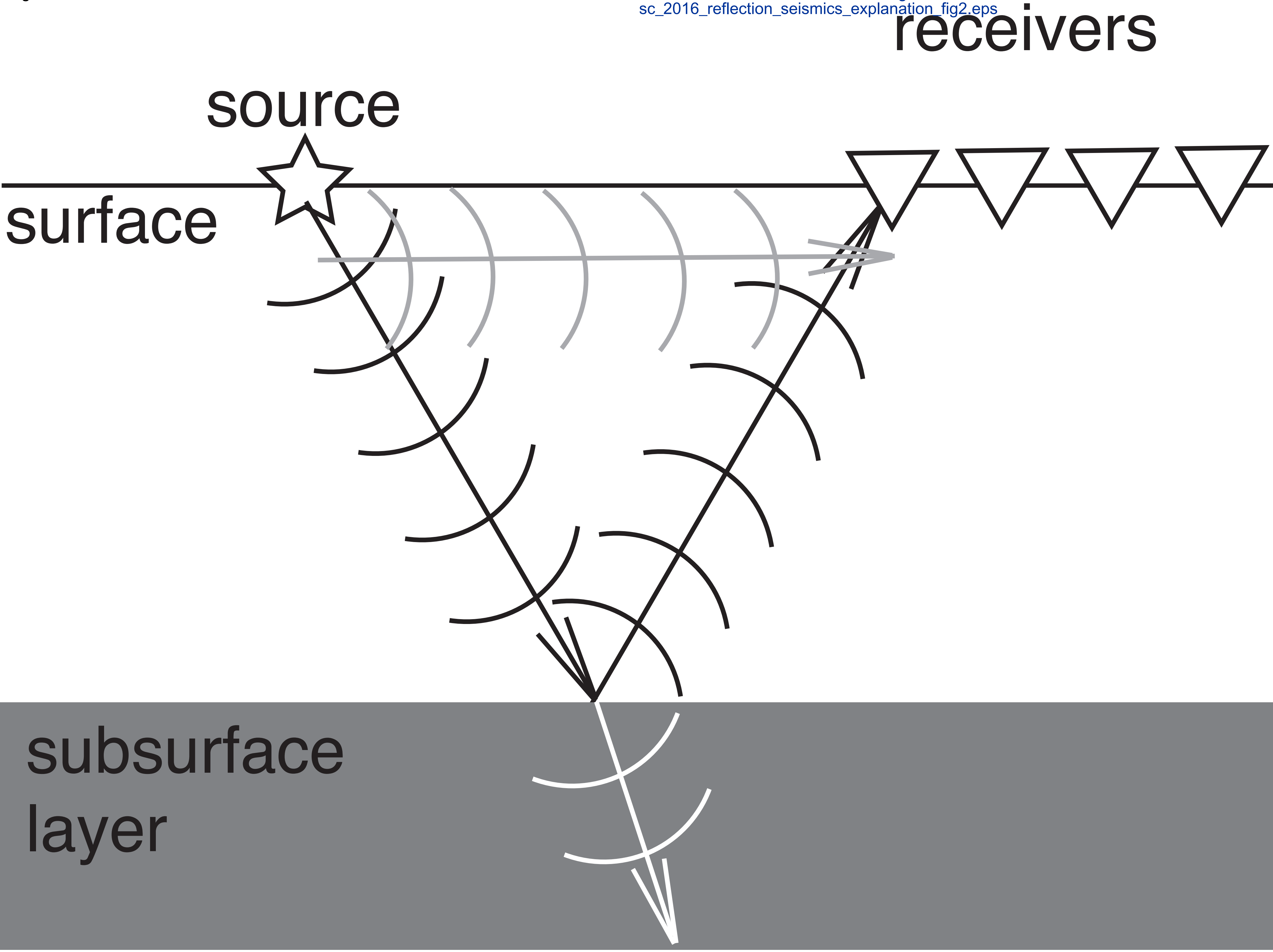

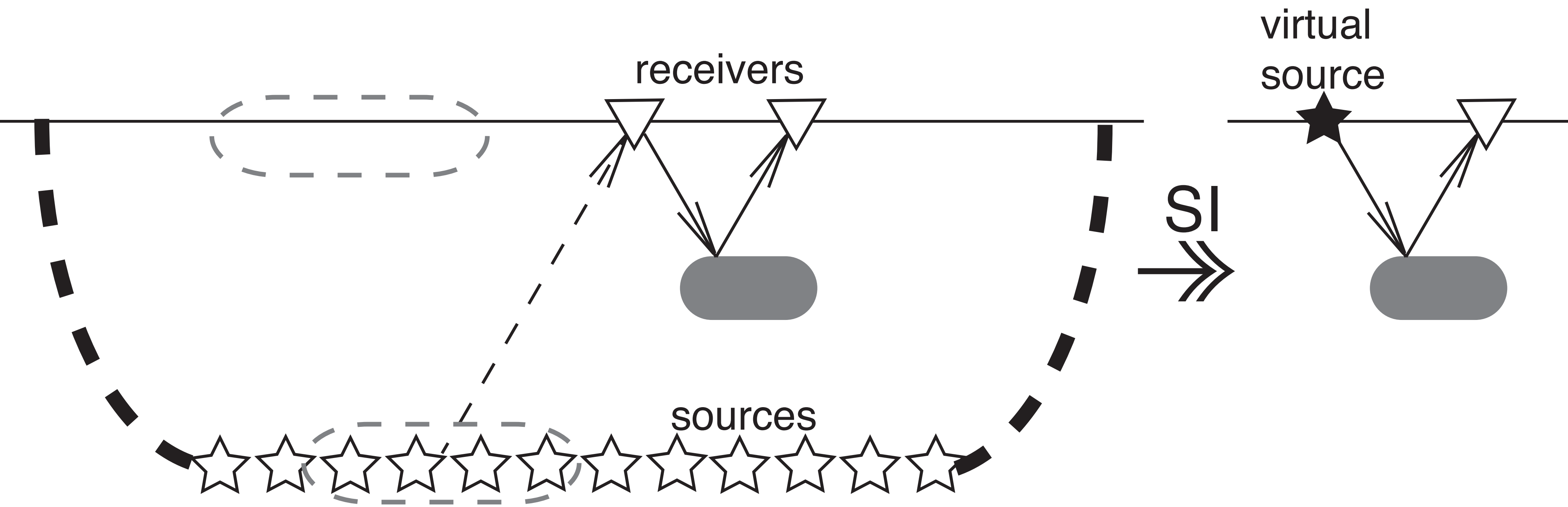
receivers
sources
SI
virtual
source

Figure 4

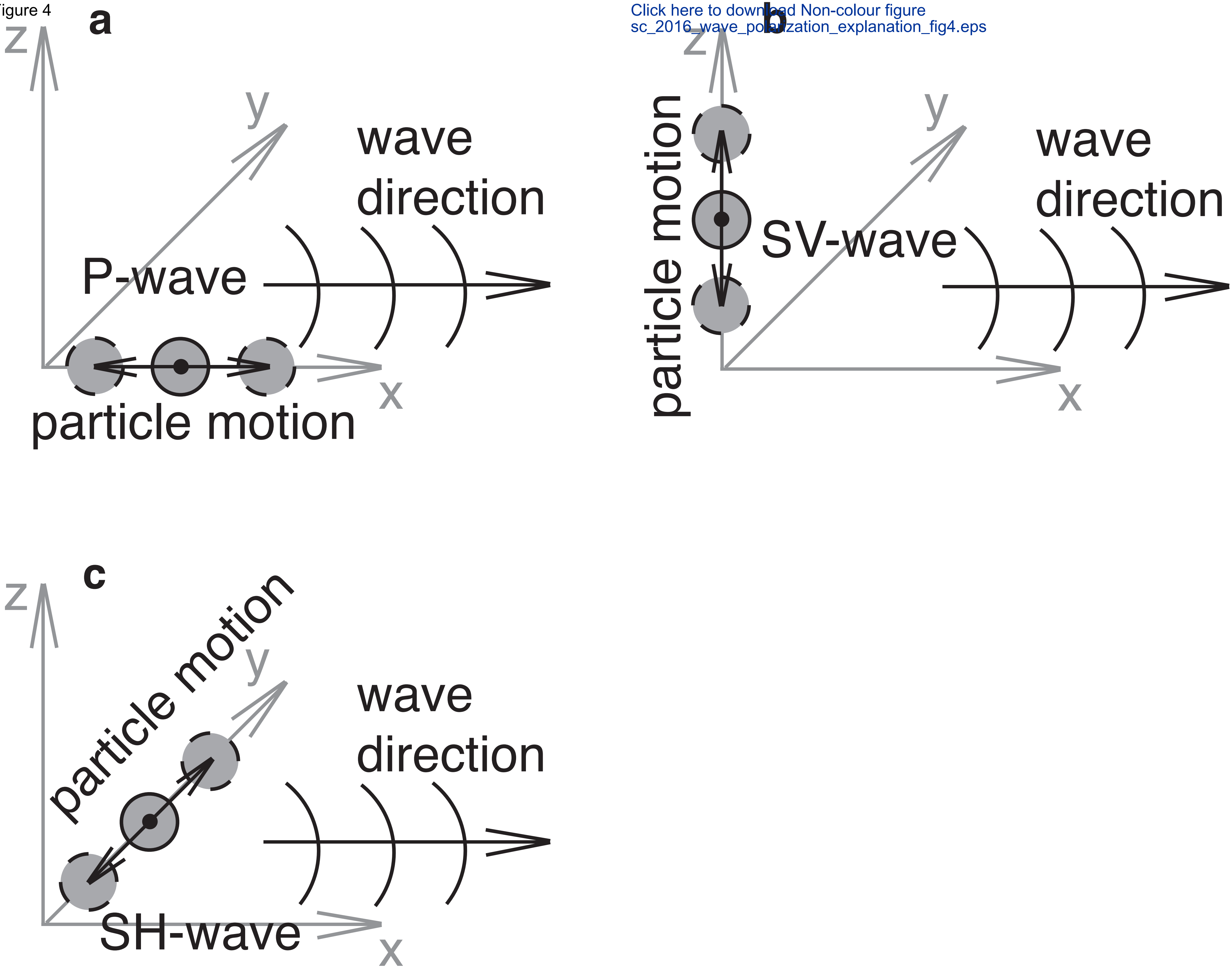
a
z
y
wave
direction
P-wave
x
particle motion
b
z
particle motion
y
wave
direction
SV-wave
x
c
z
particle motion
y
wave
direction
SH-wave
x

Figure 5

Click here to download Colour figure sc_2016_shotgathers_fig5.eps

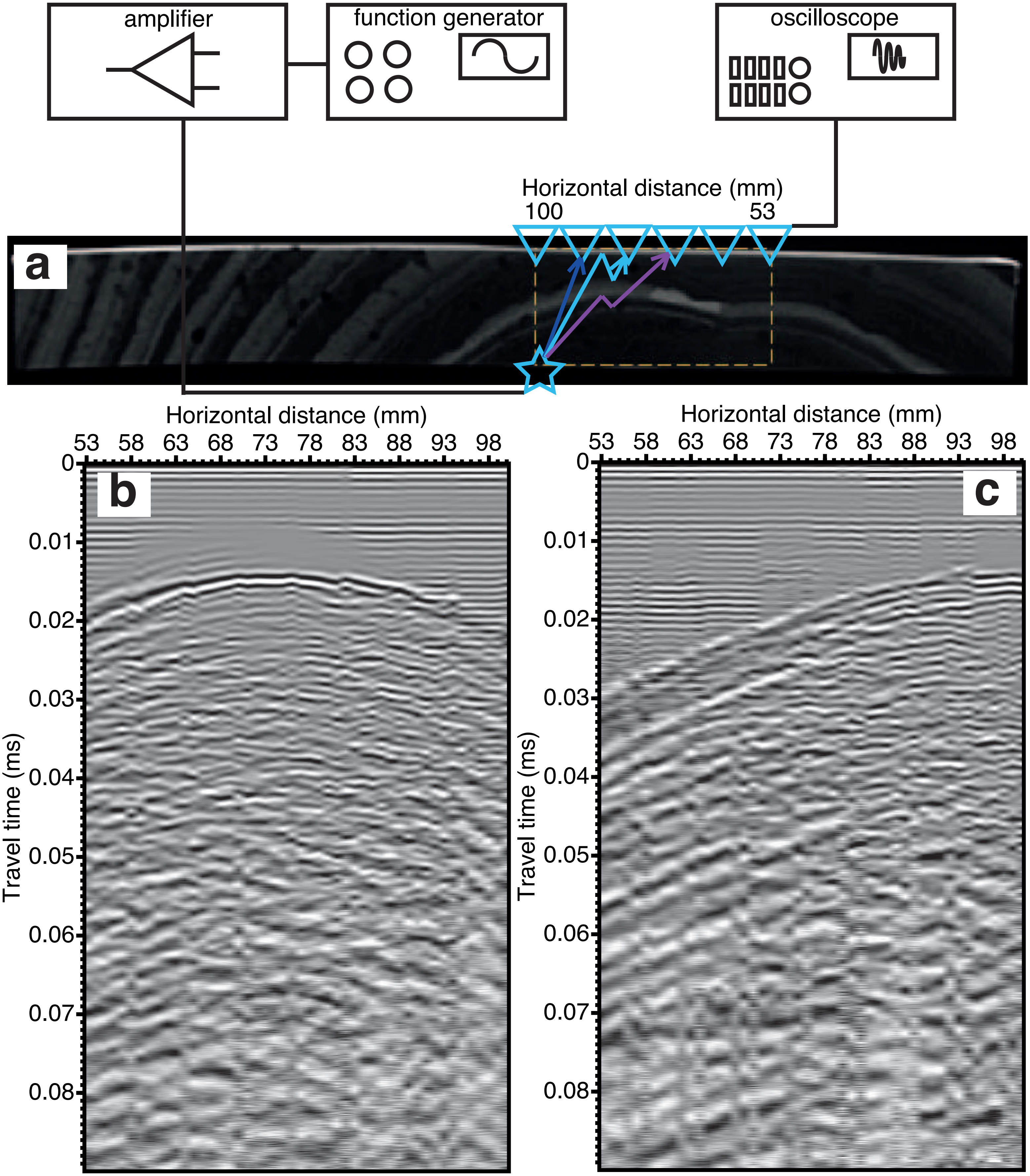

Figure 6

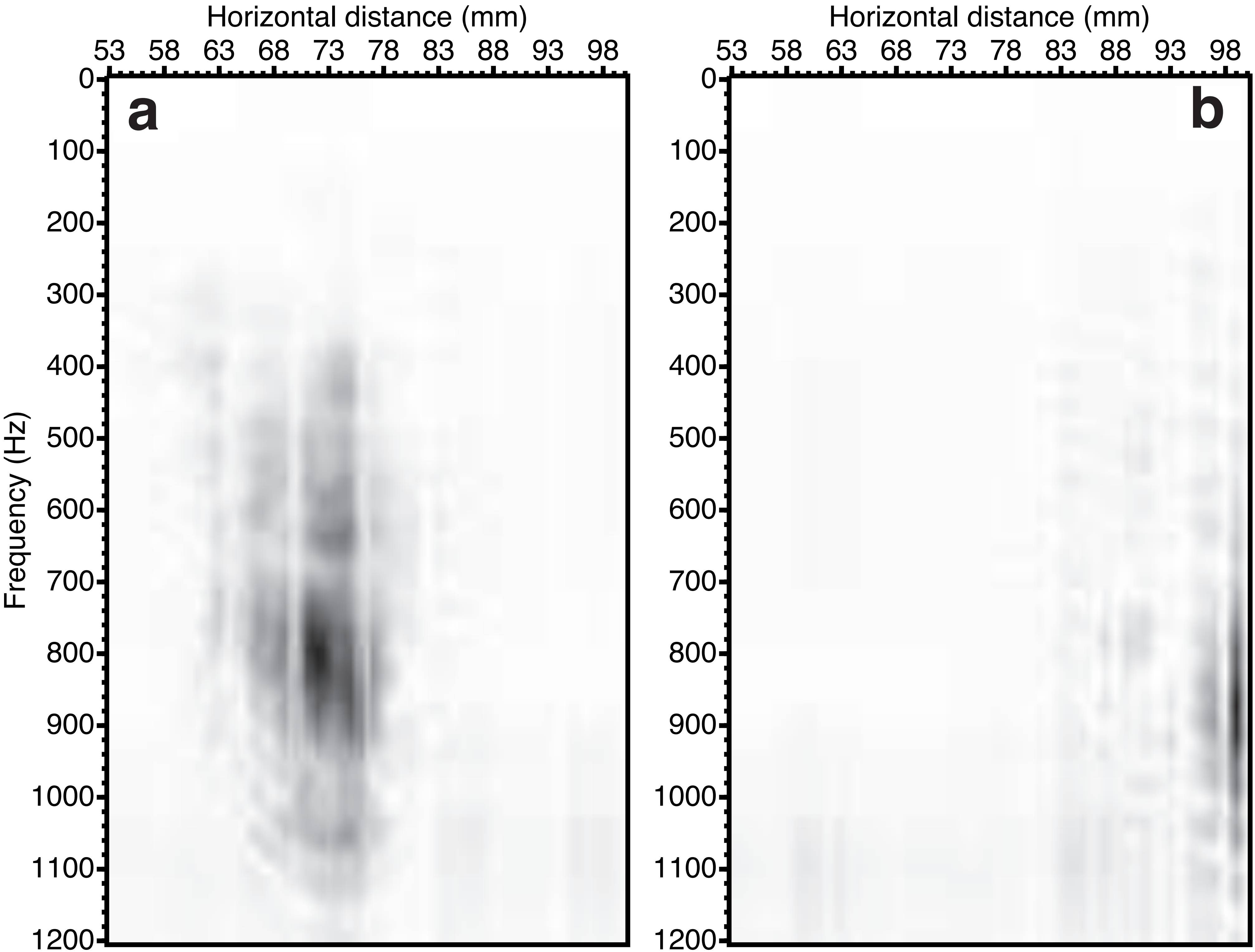
Horizontal distance (mm)
53 58 63 68 73 78 83 88 93 98
Frequency (Hz)
0 100 200 300 400 500 600 700 800 900 1000 1100 1200
a
b

Figure 7

Click here to download Non-colour figure sc_2016_modellin_mod_migr_gathers_fig7.eps

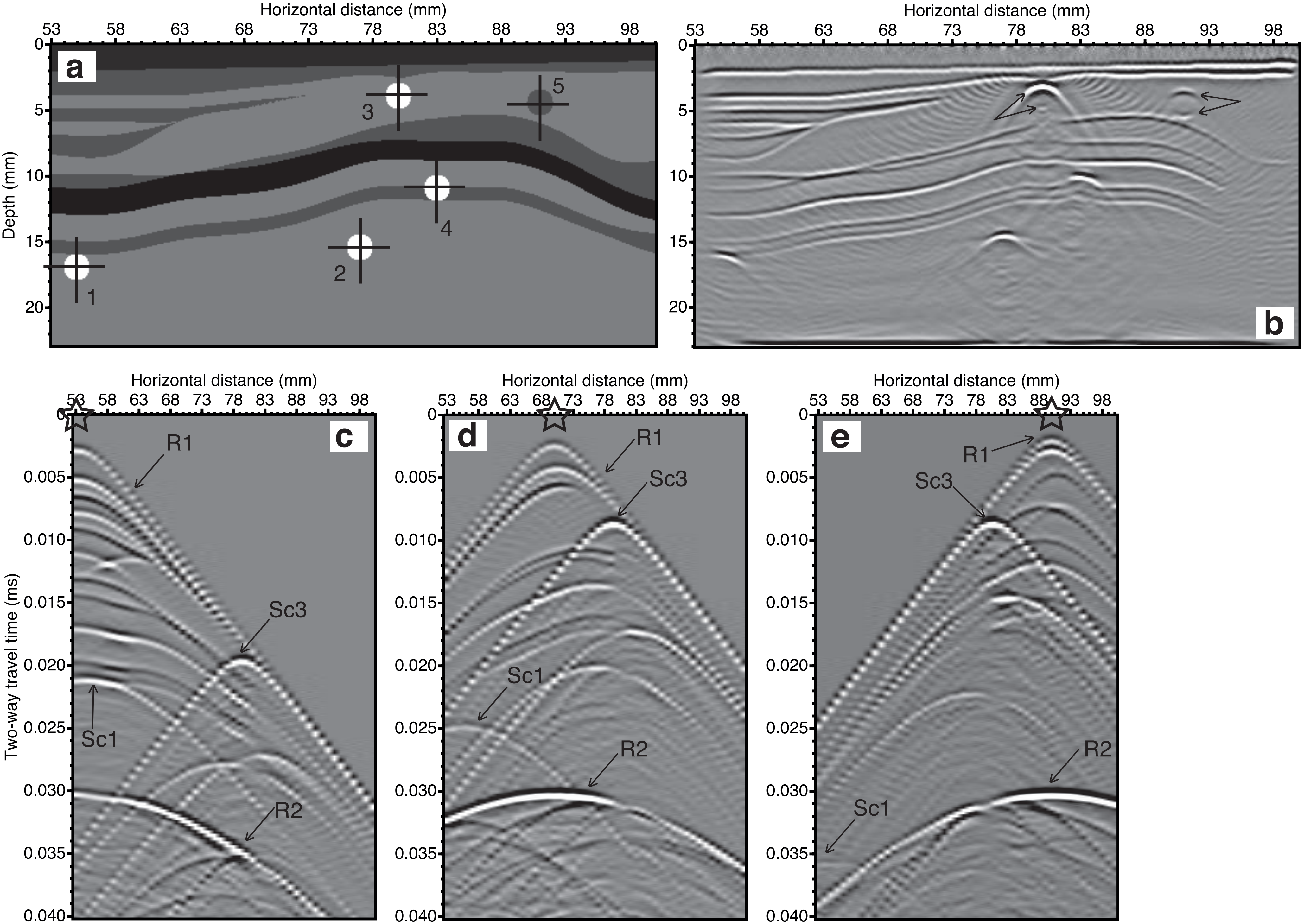

Figure 9

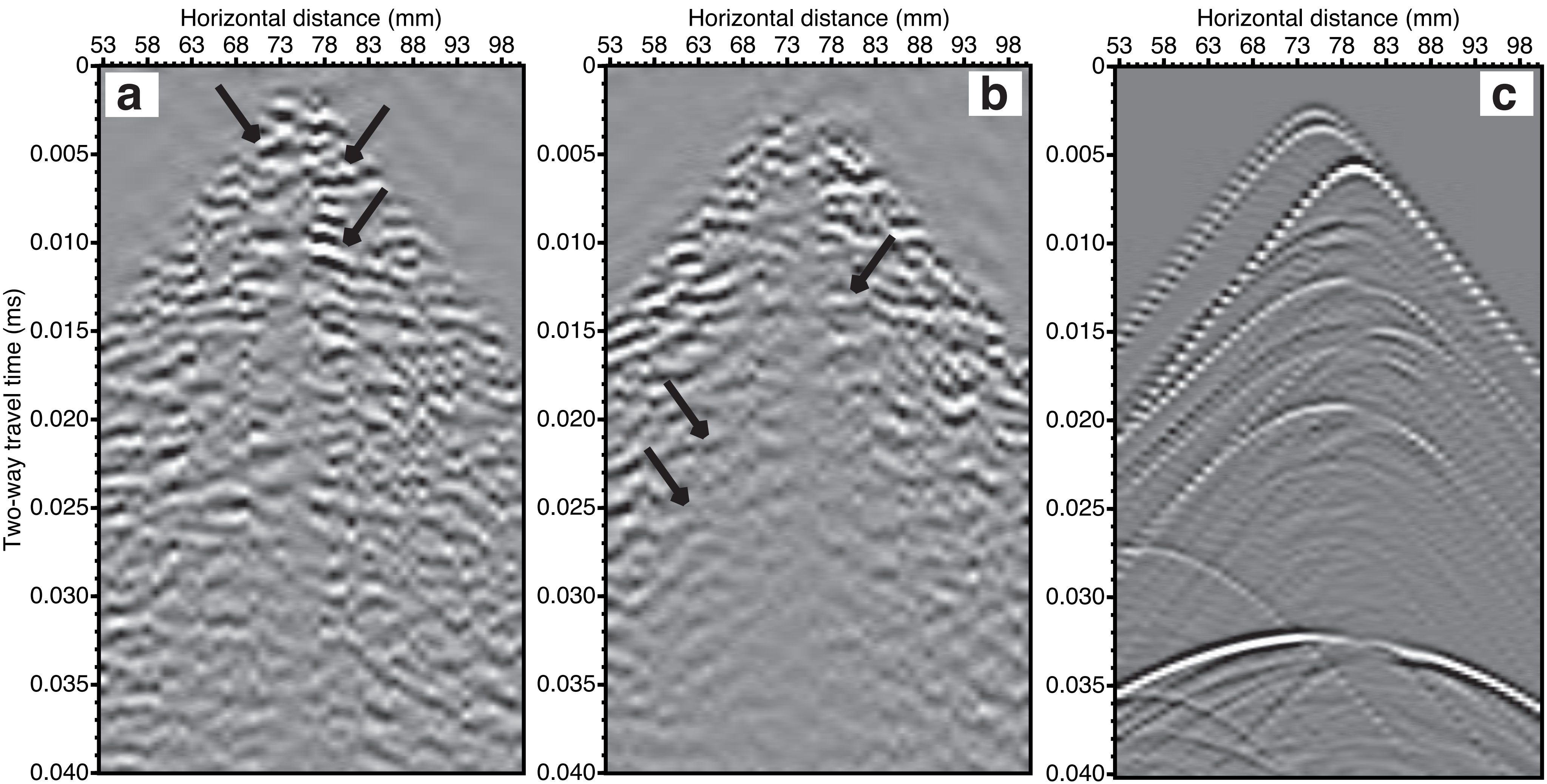

Horizontal distance (mm)
53
58
63
68
73
78
83
88
93
98
0
0.005
0.010
0.015
0.020
0.025
0.030
0.035
0.040
Two-way travel time (ms)
a
b
c

Figure 11

Click here to download Colour figure sc_2016_images_grayscale_new_fig11.eps

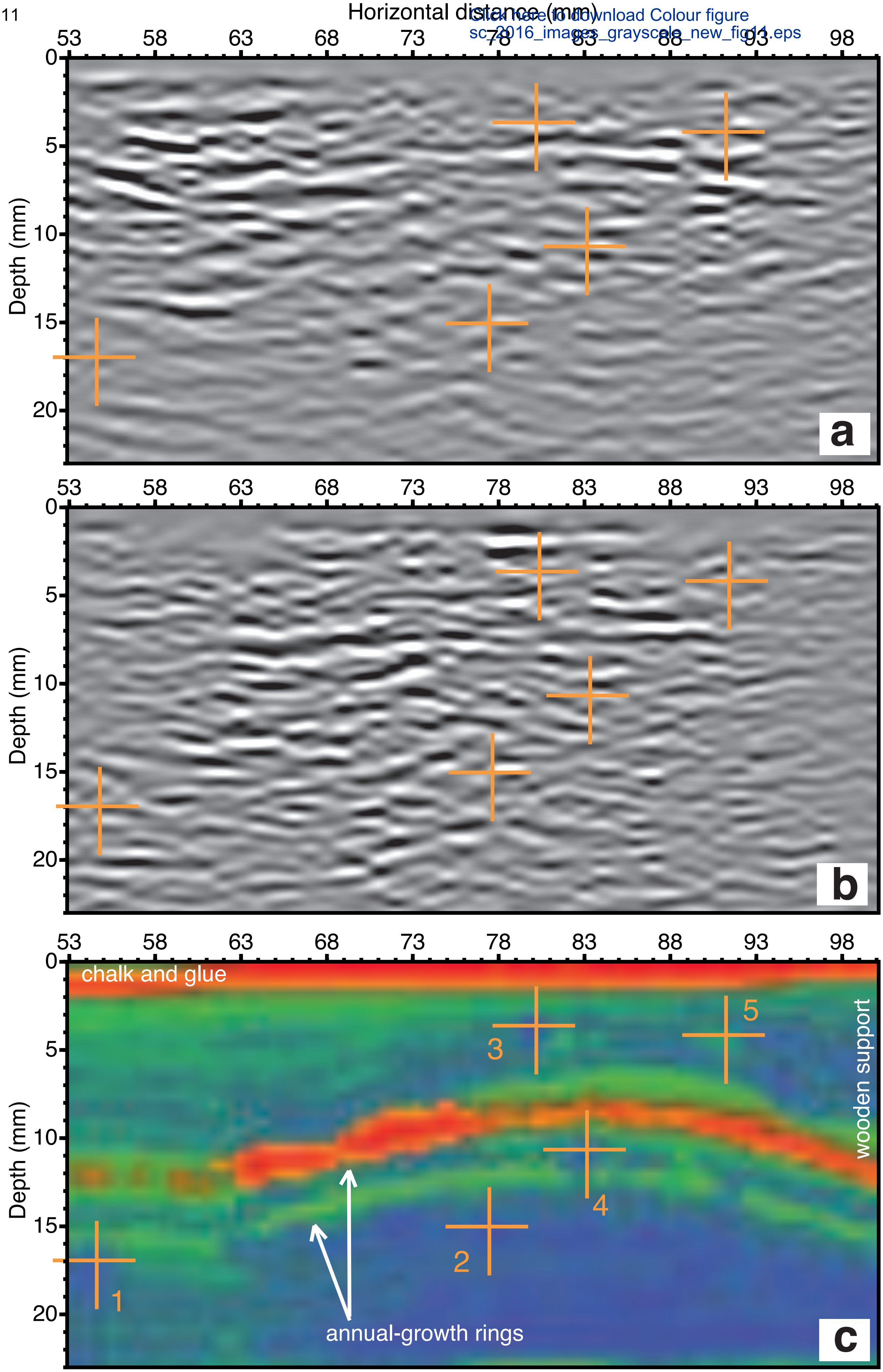

Figure 10

Click here to download Non-colour figure sc_2016_si_res_posneg_mdd_fig10.eps

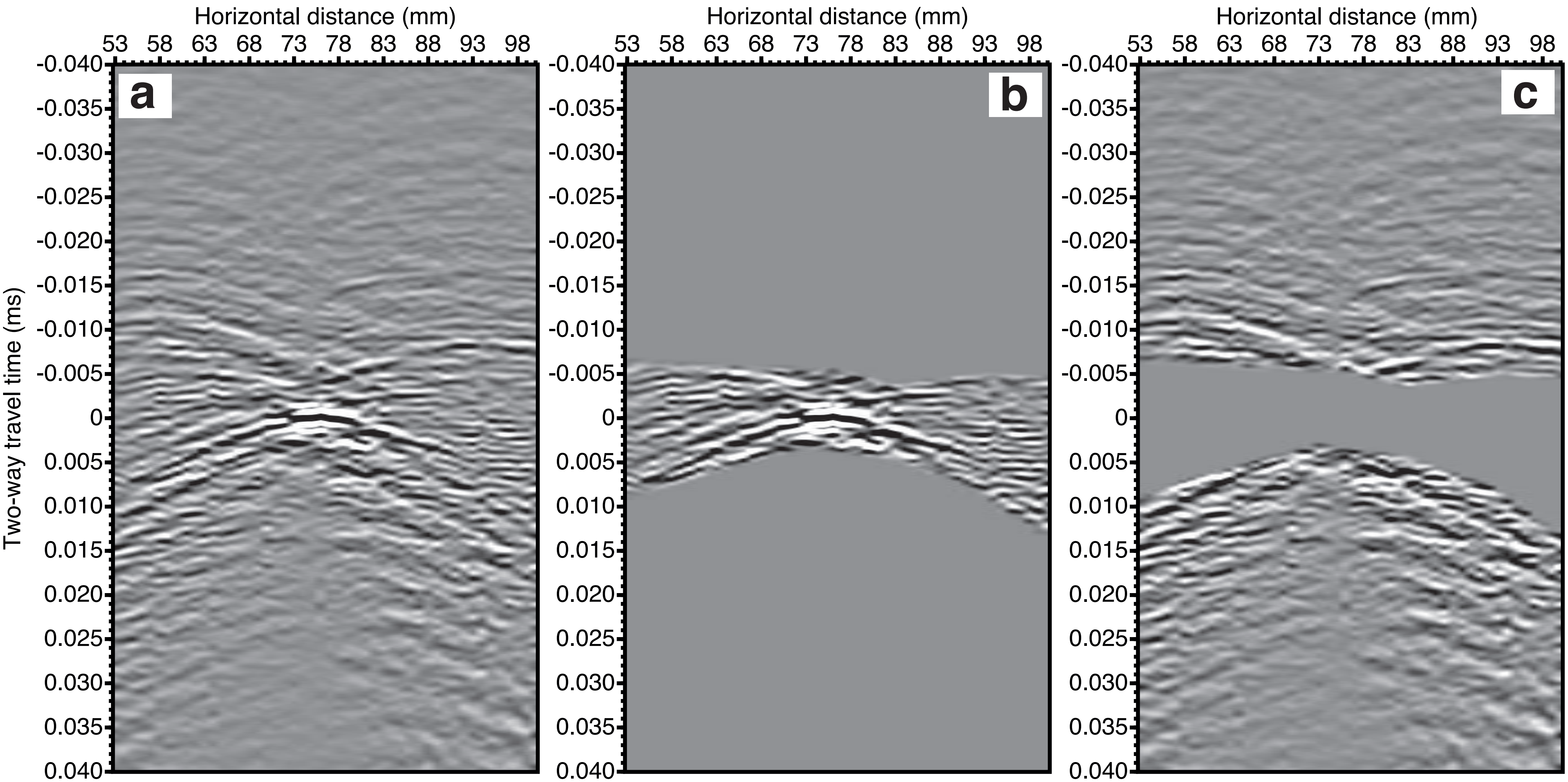

Figure 12

Click here to download Colour figure sc_2016_images_overlay_fig12.eps

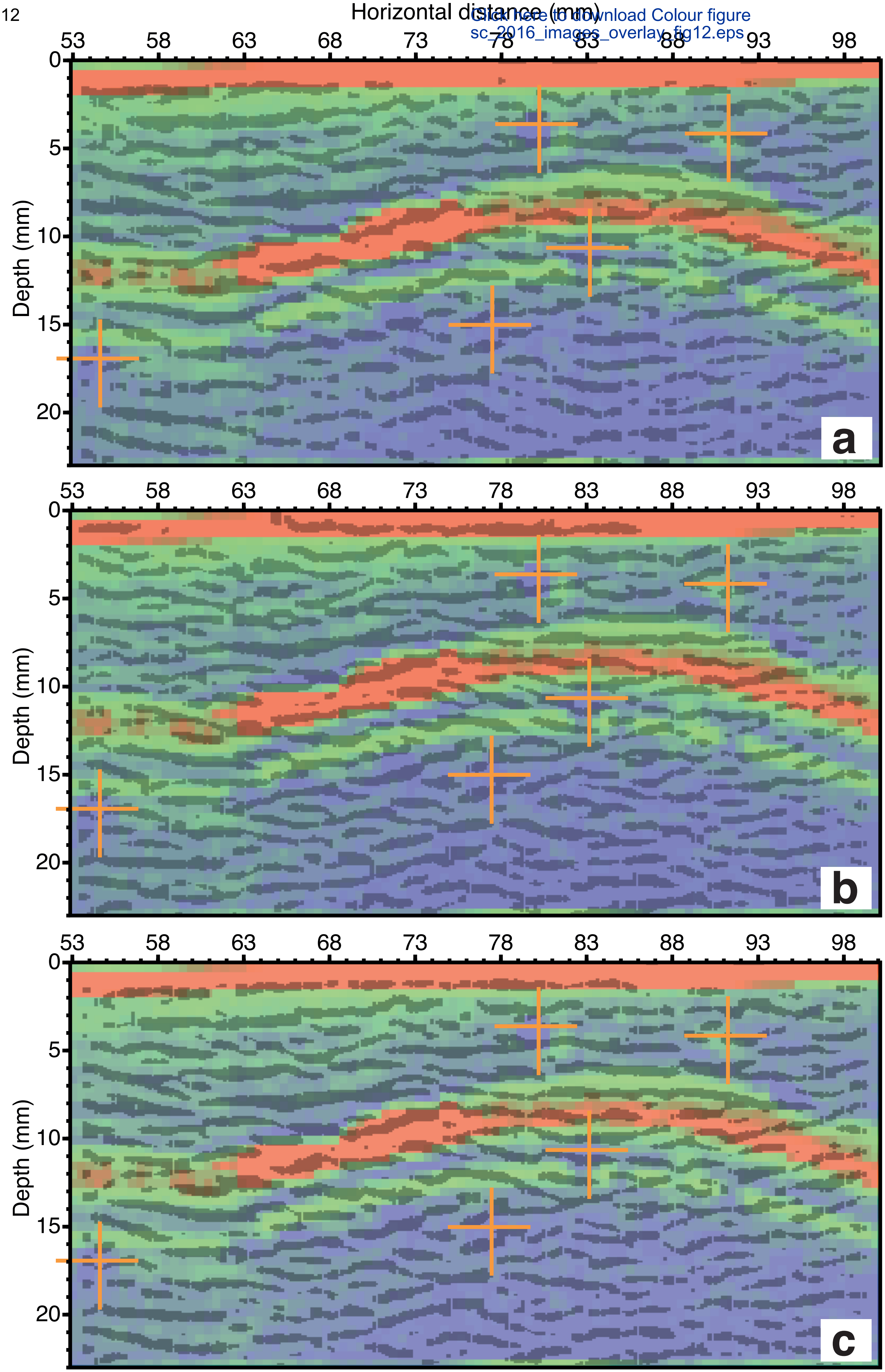

Figure 8

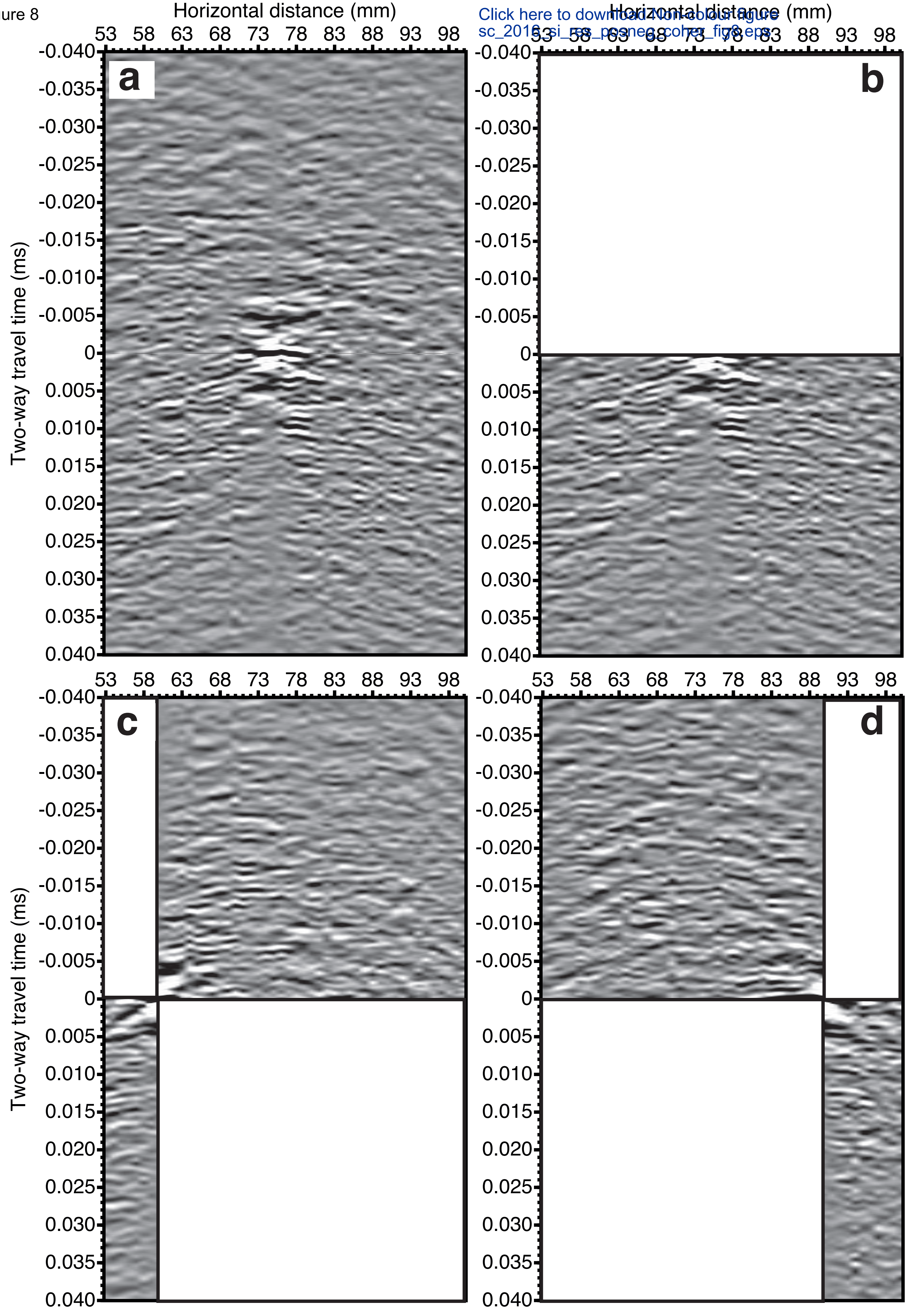

Horizontal distance (mm)
53
58
63
68
73
78
83
88
93
98
Two-way travel time (ms)
-0.040
-0.035
-0.030
-0.025
-0.020
-0.015
-0.010
-0.005
0
0.005
0.010
0.015
0.020
0.025
0.030
0.035
0.040
a
b
c
d